Science Advances
AAAS

Supplementary Materials for

Pathogenic mitochondrial DNA mutations inhibit melanoma metastasis

Spencer D. Shelton *et al.*

Corresponding author: Alpaslan Tasdogan, alpaslan.tasdogan@uk-essen.de;
Prashant Mishra, prashant.mishra@utsouthwestern.edu

Sci. Adv. **10**, eadk8801 (2024)
DOI: 10.1126/sciadv.adk8801

The PDF file includes:

Figs. S1 to S12
Legends for data S1 to S7

Other Supplementary Material for this manuscript includes the following:

Data S1 to S7

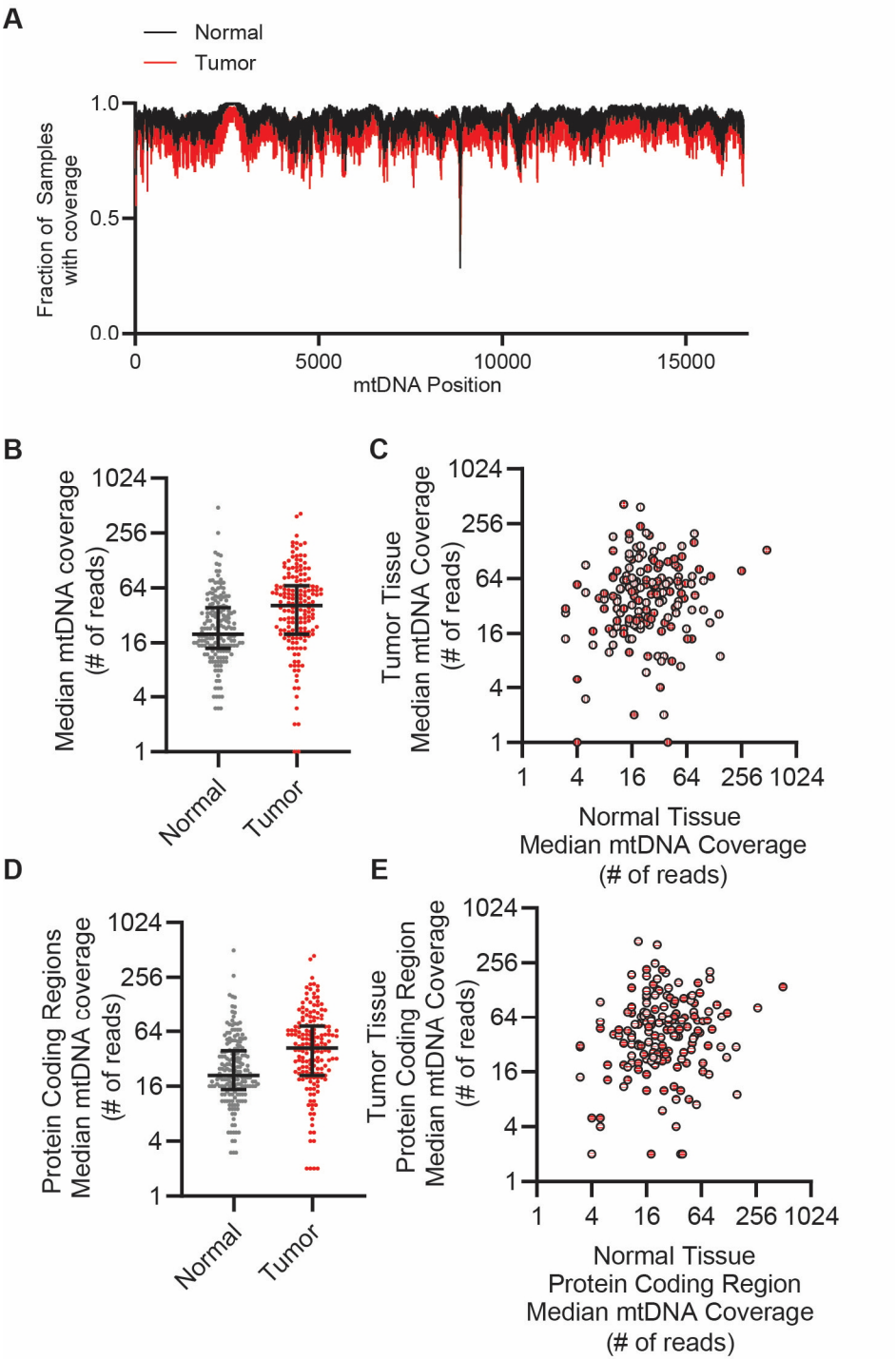

Figure S1. MtDNA read depths from melanoma and normal tissue sequencing.

A, Fractional coverage of samples with a minimum mtDNA read depth of five reads across the mitochondrial genome, comparing melanoma and normal samples.

B-C, Median mtDNA coverage for normal and tumor tissues analyzed as group (**B**) and across matched samples (**C**).

D-E, Median mtDNA coverage of the protein coding regions for normal and tumor tissues analyzed as group (**B**) and across matched samples (**C**).

Data are mean ± s.e.m from biological samples. (**B,D**).

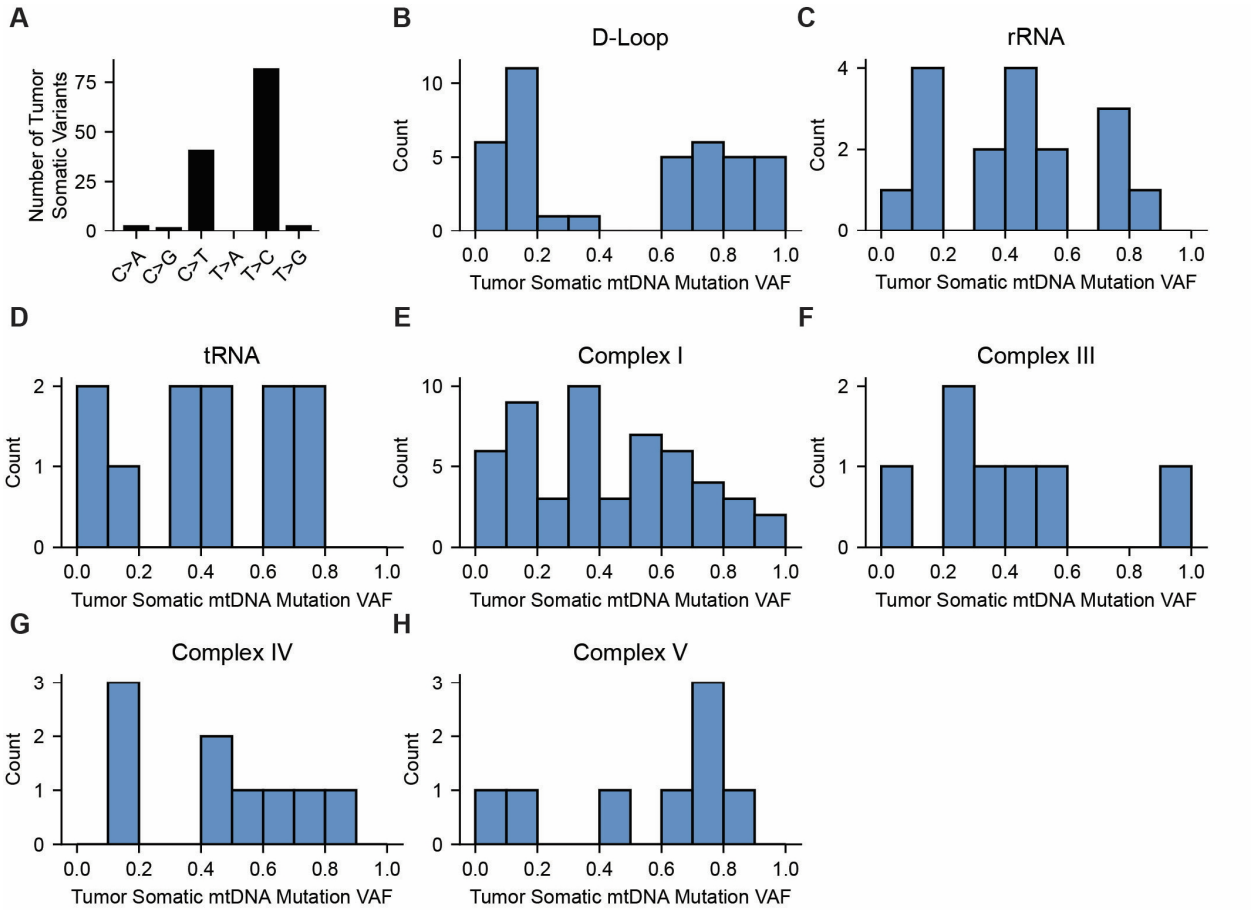

Figure S2. Mutational landscape of somatic mtDNA mutations in metastatic melanomas.

A, Somatic mtDNA mutation signature in melanomas.

B-H, Histograms of somatic variant allele frequencies (VAF) for mtDNA mutations across mtDNA regions. The x-axis represents VAF binned in intervals of 0.1, and the y-axis shows the count of detected somatic variants per bin.

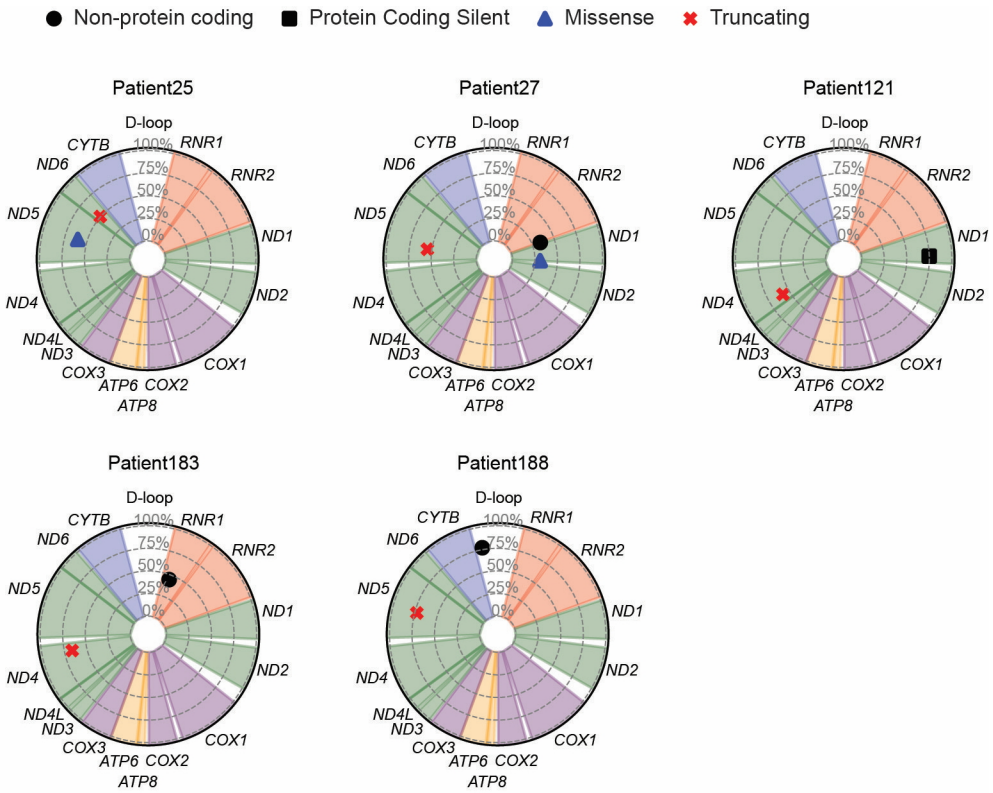

Figure S3. mtDNA mutational landscape of melanomas with somatic high VAF truncating and missense mutations.

Individual circos plots presenting all somatic mtDNA mutations identified within individual melanomas harboring at least one >0.5 VAF truncating variant. The radial depth of the circos plot, extending from the center to the outer edge, reflects the allelic fraction of each somatic allele.

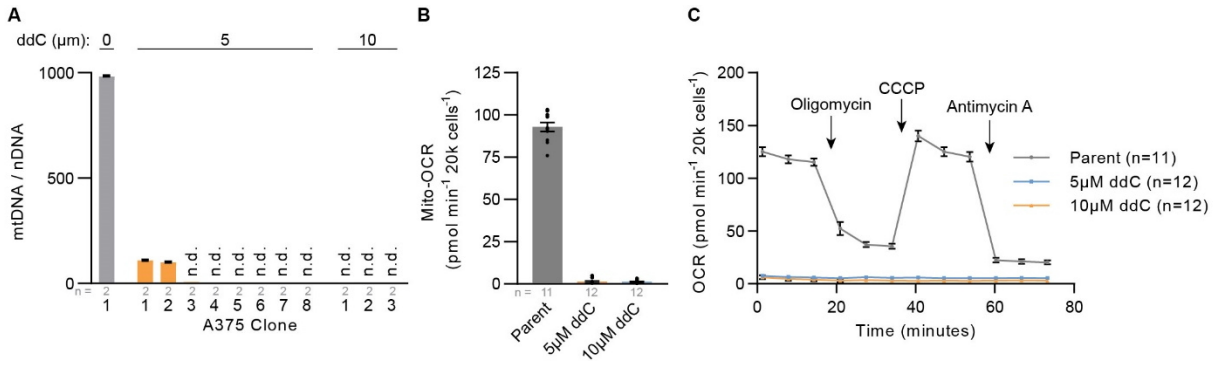

Figure S4. mtDNA depletion and establishment of ρ0 clones.

A, Mitochondrial genome (mtDNA) to nuclear genome (nDNA) ratios in A375 parental line and serial diluted clones following two week treatment with 5 μM or 10 μM ddC (dideoxycytidine). n.d., mtDNA not detected. Data from technical replicates are presented.

B,C, Mitochondrial oxygen consumption rate (mito-OCR) (**B**) and representative oxygen consumption rates (OCR) (**C**) for 20,000 cells (per well) of A375 parental line and ddC treated clones. Mitochondrial inhibitors (oligomycin, CCCP, antimycin A) were injected at the indicated timepoints. The number of samples analyzed per treatment is indicated. Data are mean ± s.e.m from biological replicates.

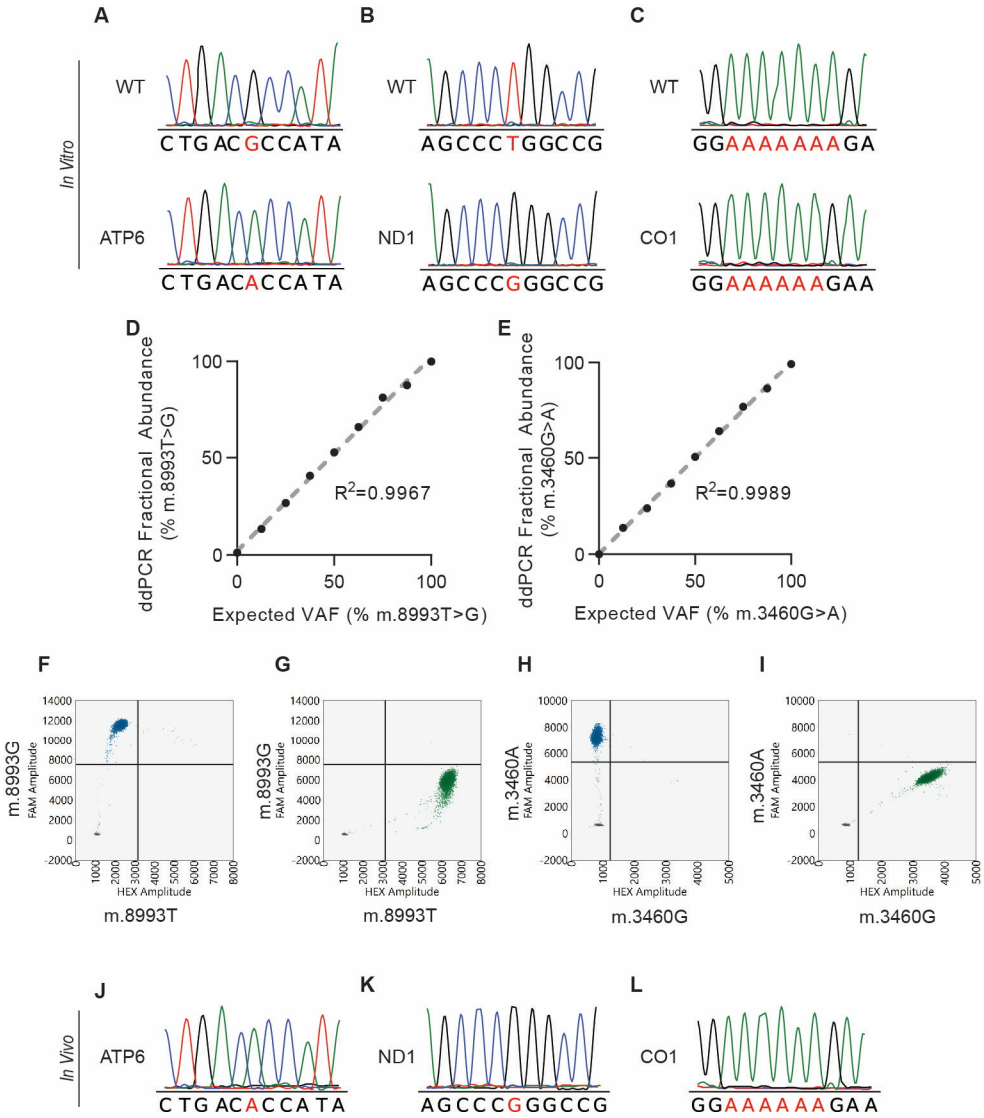

Figure S5. Genetic validation of homoplasmic A375 cybrid lines.

A-C, Representative *in vitro* Sanger sequencing of mtDNA regions surrounding positions m.8993 (**A**), m.3460 (**B**), and m.6692 (**C**) for wildtype cybrid line (top) and indicated variant cybrid lines (bottom). Pathogenic variant allelic locations are highlighted in red.

D,E, Standard curve for ddPCR probes specific to m.8993T>G (**D**) and m.3460G>A (**E**) constructed from purified plasmids for each variant. The coefficient of determination (R^2) is provided for each curve.

F,G, Representative ddPCR 2-dimensional plot with fluorescent (FAM and HEX) probes specific to the m.8993G (FAM) or m.8993T (HEX) in homoplasmic ATP6 cybrids (**F**) and wildtype cybrids (**G**).

H,I, Representative ddPCR 2-dimensional plot with fluorescent probes (FAM and HEX) specific to the m.3460A (FAM) or m.3460G (HEX) in homoplasmic ND1 cybrids (**H**) and wildtype cybrids (**I**).

J-L, Representative *in vivo* subcutaneous tumor Sanger sequencing of mtDNA regions surrounding positions m.8993 (**J**), m.3460 (**K**), and m.6692 (**L**) for indicated variant cybrid lines. Pathogenic variant allelic locations are highlighted in red.

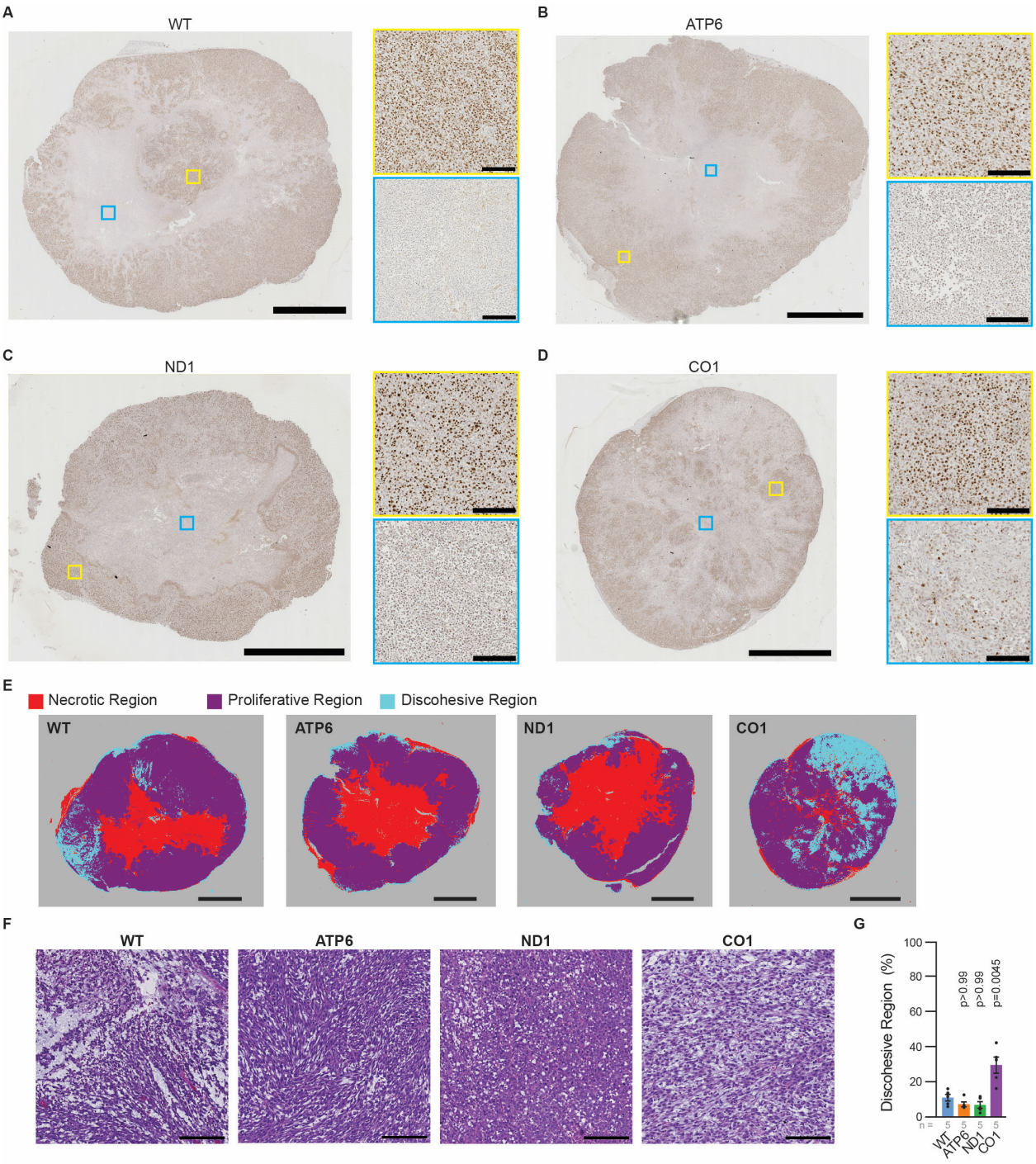

Figure S6. Histological analysis of A375 cybrid subcutaneous cybrid tumors.

A-D, Representative Ki67 staining images of xenograft subcutaneous tumors of the indicated mtDNA cybrid line. Highlighted are proliferative regions with high abundance of Ki67^{+} nuclei (top

yellow box) and non-proliferative regions with low abundance of $Ki67^+$ nuclei (bottom blue box). Scale bar for full section, 5000 μm. Scale bar for zoomed region, 200 μm.

E, Identification of tumor regions from representative H&E sections (Fig. 3E) with QuPath Analysis Pixel Classification algorithm. Scale bar, 5mm.

F,G, Representative H&E images (**F**) and cross-sectional quantitation (**G**) of discohesive regions in sections of indicated xenograft subcutaneous cybrid tumors. Scale bar, 500 μM. P values indicate comparison with WT group.

The number of tumors (biological replicates) analyzed per group is indicated. Data are mean ± s.e.m. (**G**). Statistical significance was assessed using one-way ANOVA with Dunn's multiple comparison adjustment (**G**).

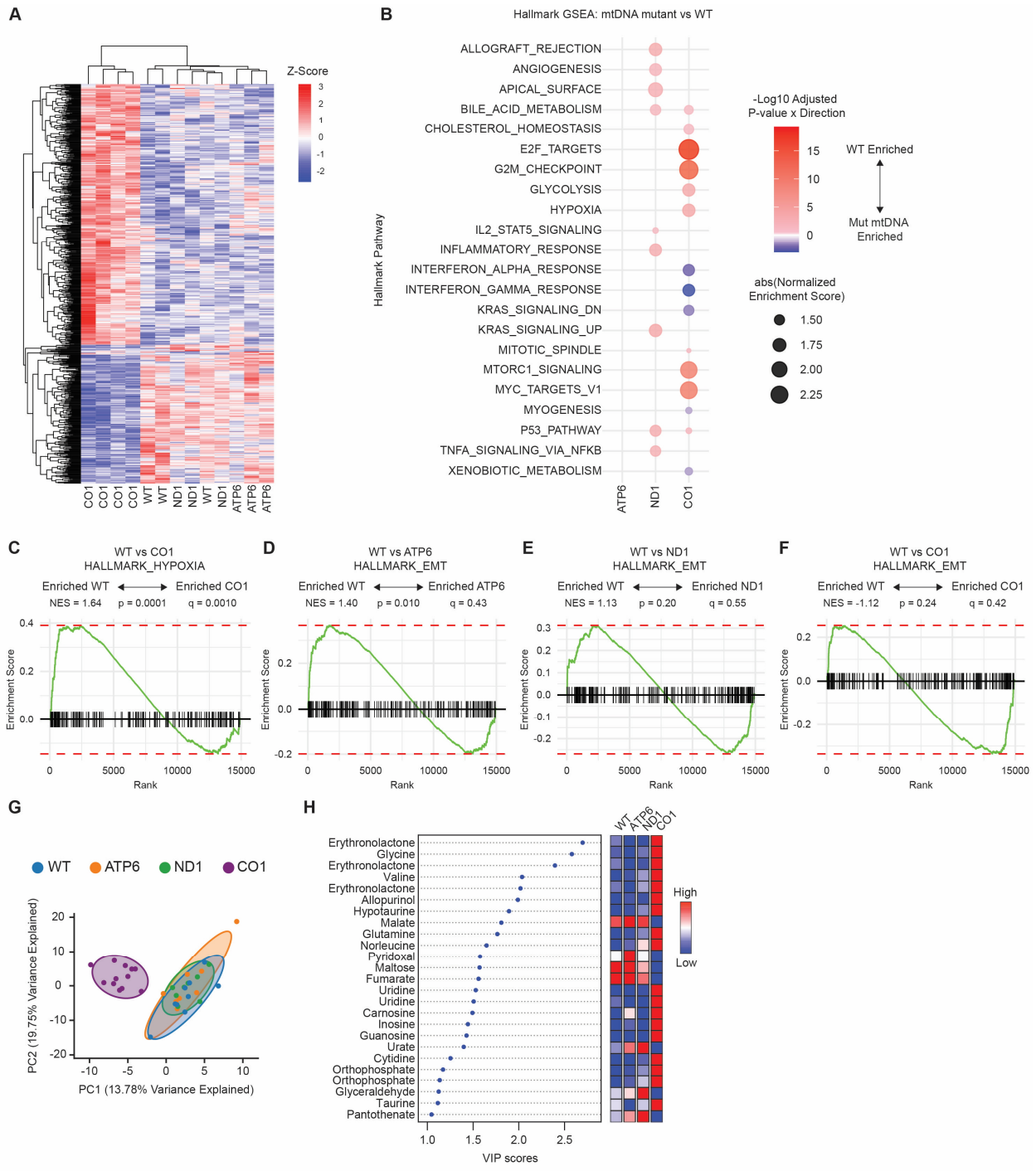

Figure S7. Transcriptional and metabolic characterization of A375 subcutaneous tumors.

A, Cluster map of significant genes from RNA sequencing of A375 subcutaneous tumors. Each gene is z-score normalized. Data is presented from biological replicates.

B, Dot plot of Hallmarks Pathway GSEA comparing WT to pathogenic cybrids. Red dots indicate pathways upregulated in WT cybrids, blue indicates pathways up in pathogenic cybrids, and dot size represents normalized enrichment scores. All represented data are filtered for q-value < 0.25.

C, Hallmarks Hypoxia pathway enrichment plot for A375 WT vs A375 CO1 subcutaneous tumors**.**

D-F, Hallmarks Epithelial-Mesenchymal-Transition (EMT) pathway enrichment plot for A375 WT vs ATP6 (**D**), WT vs ND1 (**E**), and WT vs CO1 (**F**) subcutaneous tumors.

G, PLS-DA (Partial Least Squares Discriminant Analysis) of untargeted metabolomics data from A375 subcutaneous tumors. Data are presented from biological replicates. Ovals indicate 95% confidence limits.

H, VIP (Variable importance projection) scores from nontargeted-metabolites identified by PLS-DA. Metabolites with multiple appearances were detected in various fragment patterns in the untargeted analysis (Data S7).

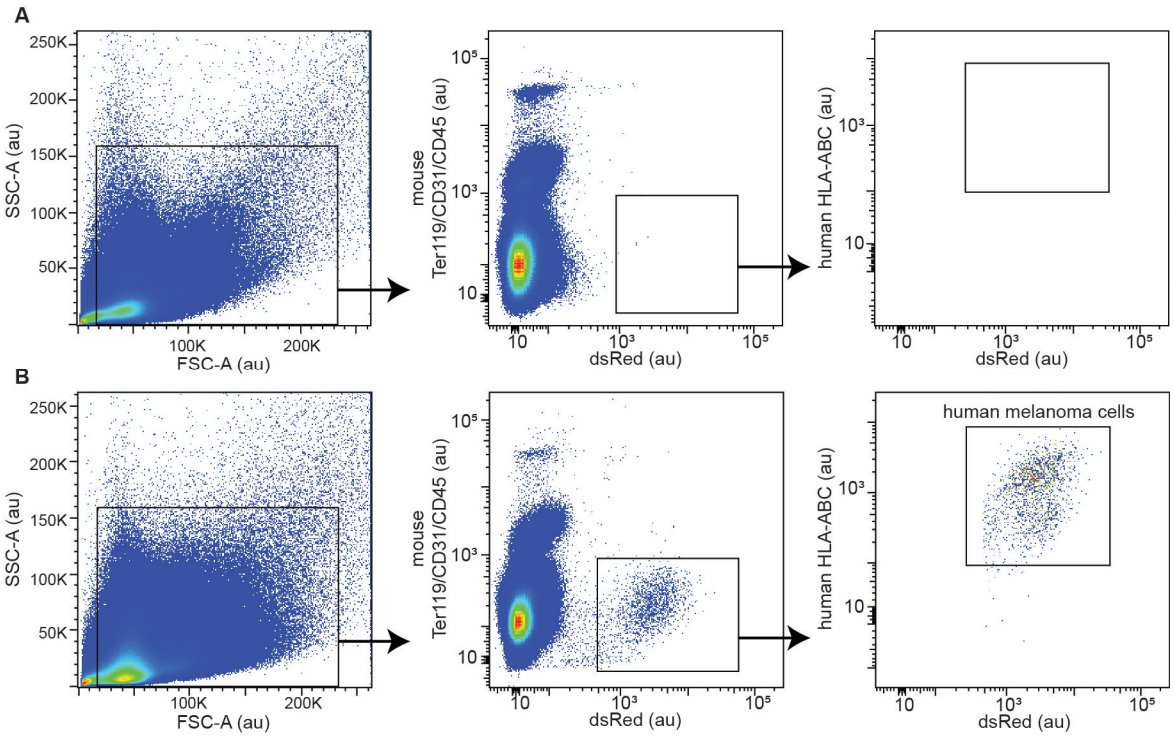

Figure S8. Isolation of circulating human melanoma cells from mouse blood.

A,B, Flow cytometric analysis and gating strategy to identify human melanoma cells in negative control mouse blood (**A**) or blood of a xenograft subcutaneous tumor bearing mouse (**B**). SSC-A, side scatter area; FSC-A, forward scatter area; au, arbitrary intensity units.

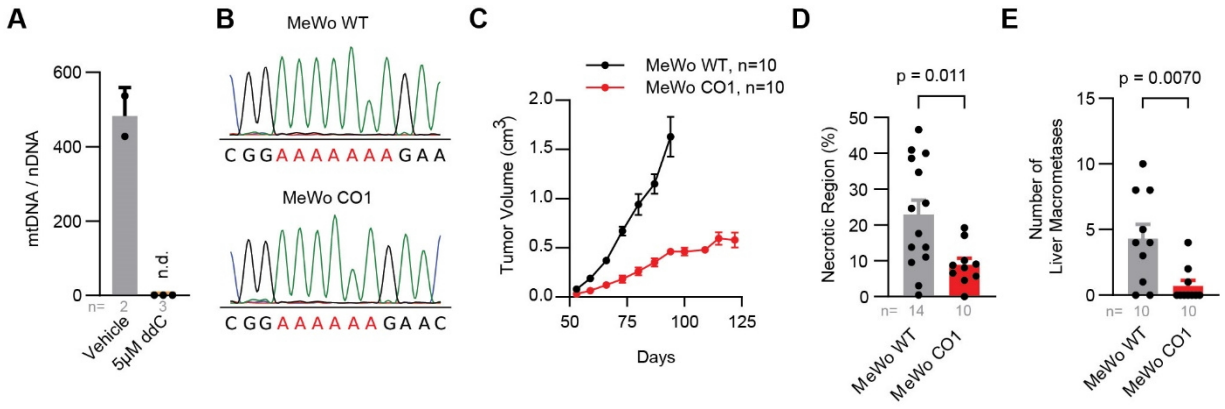

Figure S9. mtDNA with CO1 deletion diminishes tumor growth, necrosis, and metastases in the MeWo cell line.

A, mtDNA to nDNA ratios in MeWo parental line following two week treatment with vehicle or 5 μM ddC. n.d., mtDNA not detected. Data from technical replicates are presented.

B, Representative Sanger sequencing of mtDNA regions surrounding position 6692 for MeWo wildtype cybrid line (top) and CO1 cybrid (bottom). Pathogenic variant allelic locations are highlighted in red.

C, Tumor growth rate of indicated MeWo cybrid lines following 10,000 cell subcutaneous injection.

D, Quantitation of necrotic region as a percentage of tumor cross-sectional area.

E, Quantitation of liver macrometastases from indicated MeWo cybrid lines following 10,000 cell subcutaneous injection.

The number of samples (biological replicates unless indicated otherwise) analyzed per group is indicated. Data are mean ± s.e.m. (**C,D,E**). Statistical significance was assessed using unpaired t-test (**D,E**).

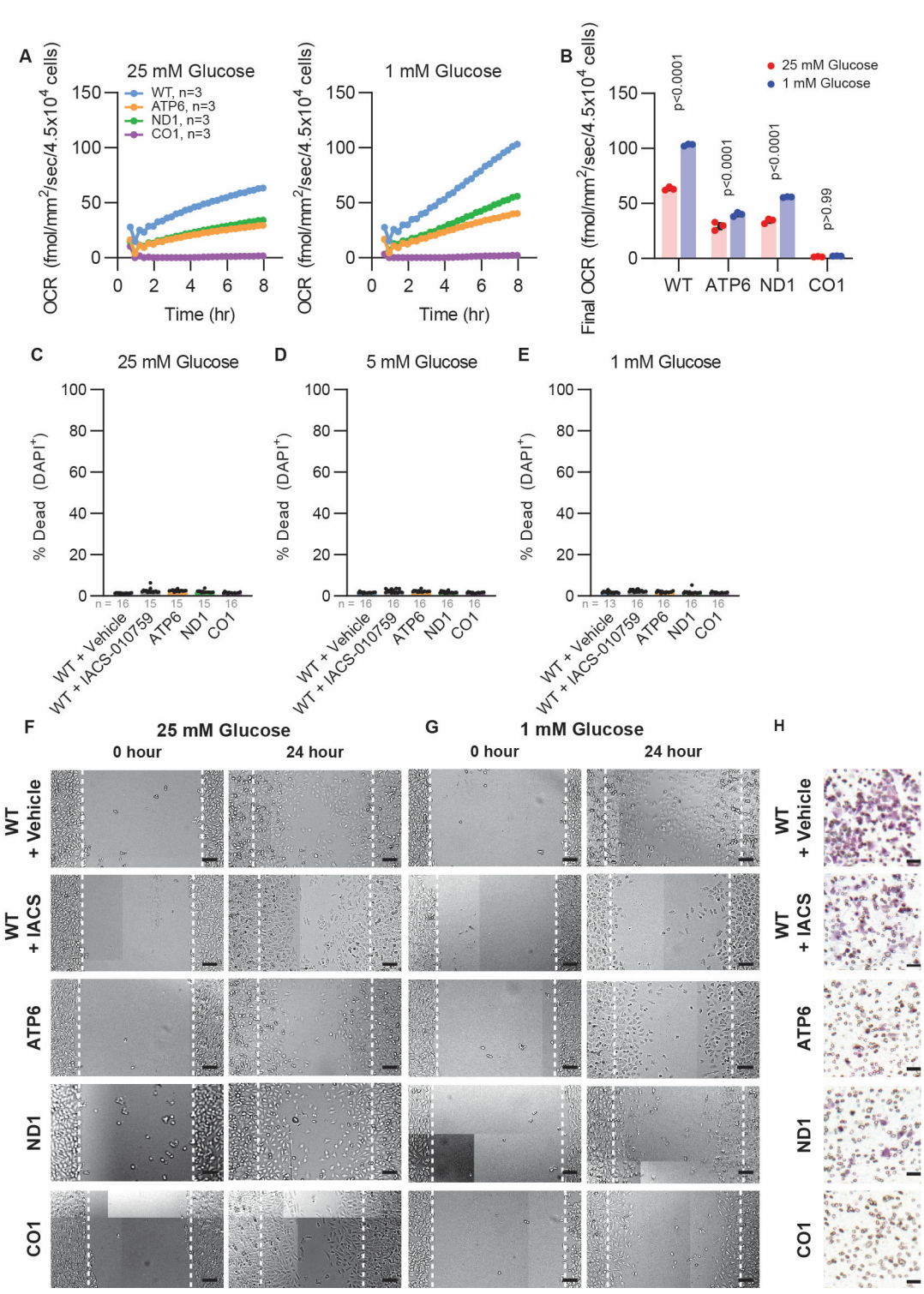

Figure S10. Reduced migration and invasion of dysfunctional cybrid lines at low glucose availability.

A,B, Continuous (**A**) and final measurement (**B**) of oxygen consumption by a monolayer culture of indicated cybrid lines at 1 mM and 25 mM glucose. P values indicate comparison of 1 mM and 25 mM oxygen consumption.

C-E, Viability for indicated cybrid lines at 25 mM (**C**), 5 mM (**D**), and 1 mM (**E**) glucose concentrations after 24 hours of culture as a confluent monolayer.

F,G, Representative wound healing migration images after 24 hours of culture in 25 mM glucose and 1 mM glucose media. Image is composed of individually stitched images with contrast enhanced for viewing purposes. Scale bar, 100 μm.

H, Representative Boyden transwell migration of cybrid cells after 24 hours of culture in 1 mM glucose media. Image contrast was enhanced for viewing purposes. Scale bar, 50 μm.

The number of samples (biological replicates) analyzed per group is indicated. Data are mean ± standard error of the mean (**A,B**) and median ± interquartile range (**C-E**). Statistical significance was assessed using two-way ANOVA with Šídák's multiple comparisons test (**B**).

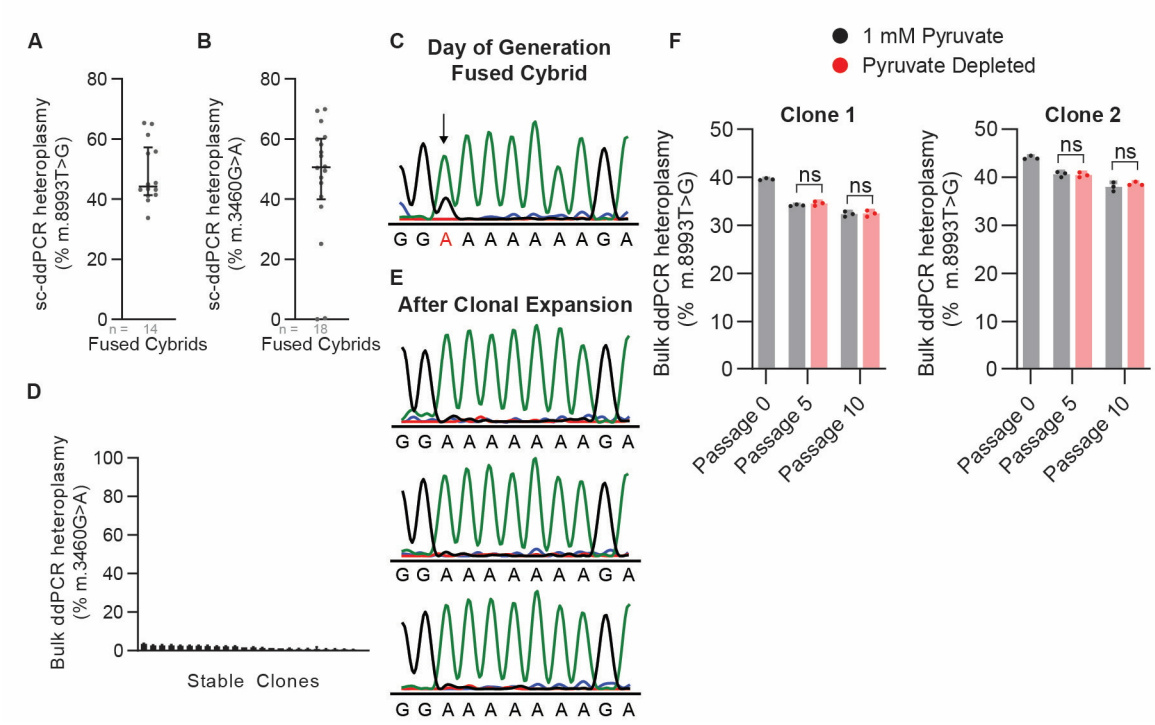

Figure S11. Heteroplasmic ND1 and CO1 alleles are lost after passage in culture while heteroplasmic ATP6 is stable in culture.

A,B, Single cell ddPCR (sc-ddPCR) analysis of heteroplasmy at *MT-ATP6* m.8993T>G (**A**) and *MT-ND1* m.3460G>A (**B**) directly following cybrid fusion of respective mutant cytoplasts with WT cybrid clones.

C, Sanger sequencing at mtDNA position m.6692 directly following cybrid fusion of CO1 cytoplasts with WT cybrid clones. Heteroplasmic allele is indicated with black arrow and red font.

D, Bulk ddPCR analysis of heteroplasmic frequency for m.3460G>A for ND1/WT cybrids after clonal line establishment. Data are presented from technical replicates.

E, Sanger sequencing at mtDNA position m.6692 for three representative CO1/WT cybrids after clonal line establishment.

F, Heteroplasmic frequency for m.8993T>G for ATP6/WT cybrids variant allele frequency following culture with 1mM pyruvate or no pyruvate supplementation at passages 0, 5, and 10.

The number of samples (biological replicates unless indicated otherwise) analyzed per group is indicated. Data are median ± interquartile range (**A,B**) and mean ± SEM (**D,F**). Statistical significance was assessed using two-way ANOVA (**F**). ns, not significant.

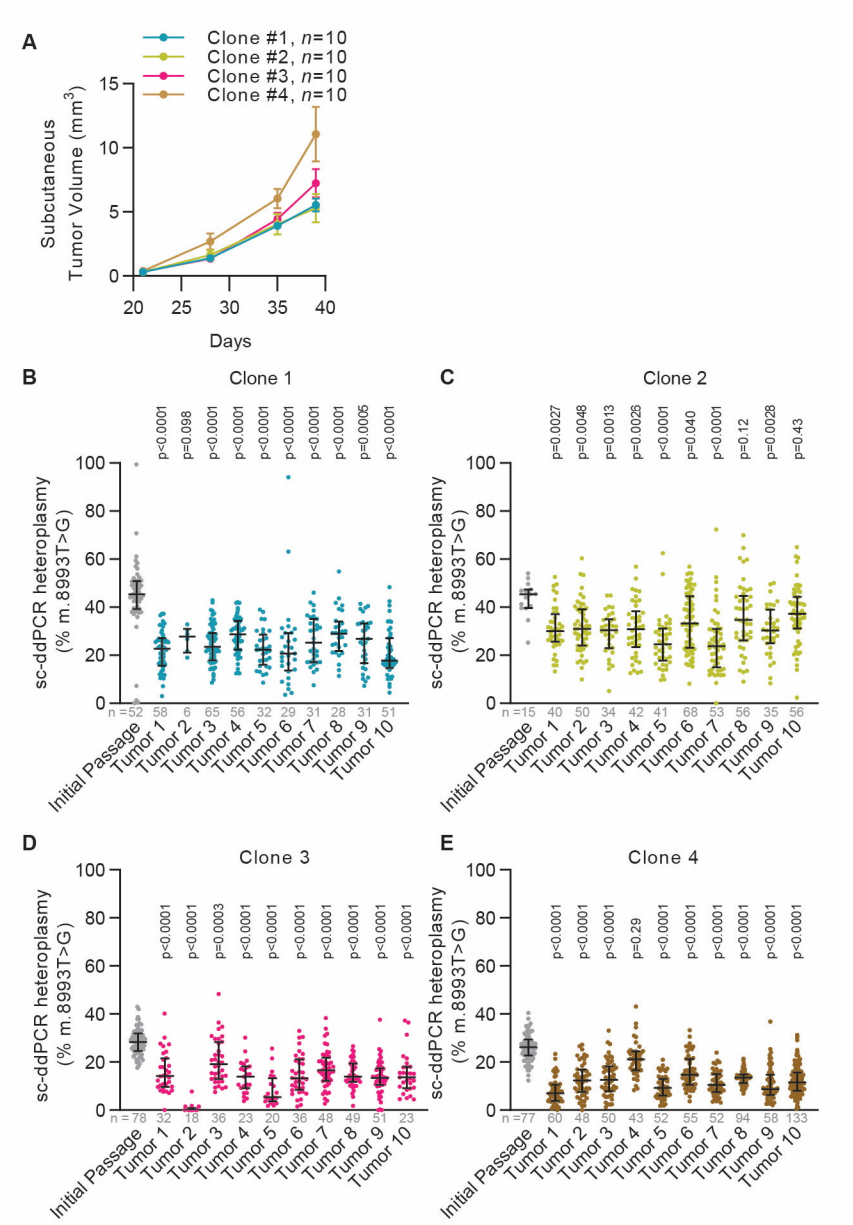

Figure S12. Heteroplasmy assessment of ATP6/WT subcutaneous tumors at increased initial subcutaneous injection cell count.

A, Subcutaneous tumor volume over time after xenograft of 10,000 cells from heteroplasmic ATP6/WT clones.

B-E, Single cell ddPCR analysis of heteroplasmic frequency for m.8993T>G for ATP6/WT heteroplasmic clones of subcutaneous xenograft of 10,000 cells following tumor growth of indicated clones. P values reflect comparisons with the initial passage.

The number of samples (biological replicates) analyzed per group is indicated. Data are median ± interquartile range (**B-E**). Statistical significance was assessed using non-parametric Kruskal-Wallis test with Dunn's multiple comparison adjustment (**B-E**).

SUPPLEMENTAL DATA

Data S1. All somatic mtDNA variants identified in human melanomas. Both normal tissue sample data and tumor data at each position is present.

Data S2. Patient mtDNA status and clinical outcomes.

Data S3. Raw RNASeq counts for A375 subcutaneous tumors.

Data S4. Genes with significant RNAseq changes as identified by DeSeq2 LRT analysis. Input was used to generate the cluster map (fig. S7A).

Data S5. GSEA results for WT vs mtDNA mutant A375 cybrid tumors from RNASeq analysis. Data was used to generate dotplot (fig. S7B).

Data S6. Raw integrated peak areas from untargeted metabolomics from A375 subcutaneous tumors.

Data S7. Metabolites with VIP scores > 1 from untargeted metabolomics and associated heatmap scores (fig. S7H).